GAMMAS 2025, Vol. 7, No. 1, p. 46–59 DOI: 10.14464/gammas.v7i1.907

International Association
of Applied Mathematics and Mechanics
– Archive for Students –

An Inverse Boundary Value Problem for the Porous Medium Equation: Numerical Methods

Lea Blessing[a,⋆], Andrea Barth[a]

[a] Institute for Applied Analysis and Numerical Simulation (IANS), University of Stuttgart, Germany
[b] IANS, University of Stuttgart, Germany

received 17.09.2025, accepted 25.11.2025, published 08.12.2025

⋆ corresponding author: lea.blessing@mathematik.uni-stuttgart.de

Abstract: *Inverse boundary value problems aim to infer a material's properties from boundary measurements. This article addresses an inverse problem for the porous medium equation, focusing on determining two coefficients characterizing the medium's diffusivity and porosity. As this problem has mainly been discussed in theory, a main contribution is the development of efficient numerical approaches for solving this problem. Based on the Dirichlet-to-Neumann map's injectivity, the diffusion coefficient's inversion can be related to the Calderón problem, leveraging its favorable properties. A key advantage of the proposed method is the decoupled inversion approach: After inferring the diffusion coefficient, the original problem only has to be solved for the porosity coefficient which can be done using a Bayesian inversion approach. This article lays the foundation for developing numerical methods solving the considered problem, highlighting the benefits of the decoupled strategy. Numerical frameworks are established for both the classical and Bayesian inversion of the diffusion coefficient. In the classical setting, noise-free measurements lead to a well-posed inverse problem. For noisy data, the Bayesian inversion maintains the problem's well-posedness.*

Keywords: inverse-problems, porous-media, Dirichlet-to-Neumann-map

1 Introduction

In many scientific fields and real-world applications, it is crucial to obtain information about quantities that cannot be observed directly but are connected to observable quantities through physical, biological or other processes. Inverse problems exploit this connection, also called the forward model, to infer the unobservable quantity of interest from available observations. An important example of such a forward model is the porous medium equation (PME). We consider the space time cylinder $Q_T := (0,T) \times Q$ and its hull $S_T := (0,T) \times \partial Q$ where $0 < T \leq \infty$ and $Q \subset \mathbb{R}^n$ is a bounded, smooth domain with $n \geq 2$. In the following, we denote $\bar{S}_T := [0,T] \times \partial Q$ if $T < \infty$ and $\bar{S}_\infty := [0,\infty) \times \partial Q$ if $T = \infty$. Furthermore, we set $L^2(Q_T) = L^2((0,T) \times Q) = L^2((0,T)) \otimes L^2(Q)$, where $\otimes$ represents the Hilbert space tensor product. The PME is defined as

$$\begin{aligned} \epsilon(x)\partial_t u(t,x) - \nabla \cdot (\gamma(x) \nabla u^m(t,x)) &= 0, && (t,x) \in Q_T, \\ u(0,x) &= 0, && x \in Q, \\ u(t,x) &= \phi(t,x), && (t,x) \in S_T, \end{aligned} \tag{1}$$

with exponent $m > 1$, gradient operator $\nabla = \nabla_x$ and non-negative boundary condition $\phi \in C(\bar{S}_T) \cap C^\infty(S_T)$. It is a degenerate parabolic type quasi-linear equation whose solution often represents a density in physical

contexts. For the existence and uniqueness of weak solutions $u \in L^\infty((0,T)) \otimes L^\infty(Q)$ of the PME, we refer to [7]. The behavior of the solution is governed by two coefficients $\epsilon, \gamma \in C^\infty(\bar{Q})$ characterizing the porosity and the diffusivity of the medium. They are assumed to be bounded with a strictly positive lower bound. In general, the degeneracy of the PME poses a significant difficulty, both theoretically and numerically, as it prohibits the application of many standard results and techniques for parabolic equations, see for example [19, Part III-VI] or [11]. Our goal in the following is to solve an inverse boundary value problem (IBVP) for the PME. IBVPs are a special class of inverse problems where the unknown quantity of interest on the entire domain is inferred from boundary observations only. In our case, we aim to reconstruct the unknown porosity and diffusion coefficient ϵ and γ from the knowledge of the Dirichlet-to-Neumann (DN) map

$$\Lambda^{PME}_{\epsilon,\gamma}(\phi) := \gamma \partial_\nu u^m|_{[0,T)\times\partial Q}, \tag{2}$$

for suitable boundary conditions ϕ and where ∂_ν denotes the boundary derivative with respect to the outwards pointing unit normal vector. The injectivity of the DN map in the following theorem is an important theoretical result for the well-posedness of our IBVP and is based on the approach of Cârstea et al. [7].

Theorem 1. *Let $T = \infty$ and let $\phi \in C(\bar{S}_\infty) \cap C^\infty(S_\infty), \phi \geq 0$ be of the form $\phi(t,x) = \chi(t) g(x)^{\frac{1}{m}}$ for $(t,x) \in S_\infty$ with $g \in C^\infty(\partial Q), g \geq 0$ and an arbitrary but fixed function $\chi \in C^\infty([0,\infty))$ which is increasing and fulfills $\chi(t) = 0$ for $t \leq \frac{1}{2}$ and $\chi(t) = 1$ for $t \geq 1$. If $\Lambda^{PME}_{\epsilon,\gamma}(\phi) = \Lambda^{PME}_{\epsilon^*,\gamma^*}(\phi)$ for all such ϕ, then $\epsilon^* = \epsilon$ and $\gamma^* = \gamma$.*

The proof can be found in the supplementary material. In the following, we denote the unknown true diffusion and porosity coefficients by ϵ^* and γ^*. While the first IBVPs have originally been formulated for elliptic boundary value problems [6], this concept has since been expanded to various other boundary value problems, including semi-linear elliptic and parabolic equations, quasi-linear elliptic equations, degenerate elliptic equations and the PME, see for example [10], [12], [4] and [7] , respectively. Numerous approaches for solving elliptic IBVPs already exist in the literature, including methods based on scattering transforms, e.g. [9], methods using integral equations, e.g. [1], and factorization methods, e.g. [5]. There have also been established reconstruction methods, e.g. [8], and linear-type sampling methods, e.g. [17], for parabolic IBVPs. Numerical methods treating the IBVP for the PME are scarce in the existing literature to the best of our knowledge. We propose a numerical approach which decouples the inverse problem for the diffusion and porosity coefficients, tying the inversion of the diffusion coefficient back to an elliptic IBVP. This leads to a significant reduction of computational effort when solving the IBVP numerically. We proceed as follows: section 2 focuses on the decoupling of the inversion tasks. Consequently, we consider the inversion of the diffusion coefficient in section 3 and of the porosity coefficient in section 4 separately.

2 Decoupling of Inversion Tasks

Our goal for this section is to identify a new IBVP for the diffusion coefficient which is independent of the porosity coefficient and thus enables us to infer both coefficients consecutively rather than simultaneously. Assuming the requirements of Theorem 1 are satisfied, we define the quantity

$$\lambda(g) := \lim_{h\to\infty} \frac{\int_0^\infty \mathrm{e}^{-\frac{t}{h}} \Lambda^{PME}_{\epsilon^*,\gamma^*}(\chi g^{\frac{1}{m}})\, dt}{\int_0^\infty \mathrm{e}^{-\frac{t}{h}} \chi^m(t)\, dt}, \tag{3}$$

which captures the boundary response corresponding to the boundary condition g, averaged over time. According to the following lemma, this represents the DN map of a well-known elliptic IBVP.

Lemma 2. *Let the assumptions from Theorem 1 be satisfied, let $\phi = \chi g^{\frac{1}{m}}$ be the boundary conditions of the PME and let the DN map $\Lambda^{PME}_{\epsilon^*,\gamma^*}(\chi g^{\frac{1}{m}})$ be given. We consider the elliptic equation*

$$\begin{aligned} \nabla\cdot(\gamma(x)\nabla v(x)) = 0, &\qquad x \in Q, \\ v(x) = g(x), &\qquad x \in \partial Q, \end{aligned} \tag{4}$$

with DN map $\Lambda_\gamma(g) := \gamma \partial_\nu v|_{\partial Q}$. Then the quantity from equation (3) represents this DN map, that is

$$\Lambda_{\gamma^*}(g) = \lambda(g). \tag{5}$$

For the proof, we refer to the supplementary material. Note that this DN map is linear and continuous with respect to the boundary data g, see [7], [16] or [20]. The task to determine the diffusion coefficient from the knowledge of the DN map $\Lambda_{\gamma^*}(g)$ for suitable boundary conditions g is also known as the Calderón problem [6]. Similar to the DN map of the PME, the Calderón DN map is also injective with respect to γ, as proven by Sylvester and Uhlmann [20]. Figure 1 illustrates the new inversion approach that can be derived from Lemma 2. It allows us to decouple the inverse problem into two sequential steps, recovering the diffusion coefficient first and the porosity coefficient afterwards. The unknown

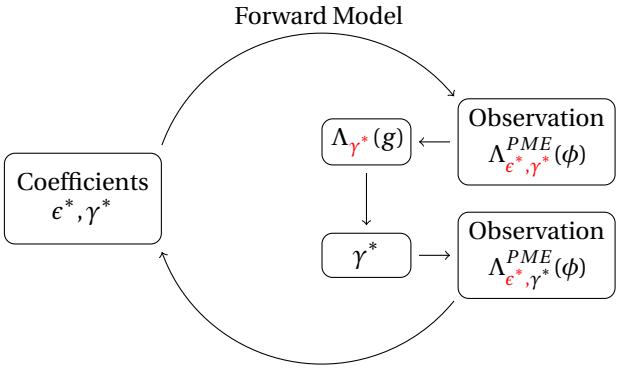

Figure 1 – Decoupled inversion approach.

quantities in each step are highlighted in red. Since we are able to obtain the Calderón data from the available PME data according to Lemma 2, we first solve the Calderón problem to determine the diffusion coefficient. Afterwards, we solve the original inverse problem for the porosity coefficient alone. Through the decoupling of the inversion tasks and by identifying a less challenging problem for the diffusion coefficient than the PME itself, we reduce the computational effort significantly. In the following, we assume the diffusion and porosity coefficients to be parametric and that they can be identified with p-dimensional parameter vectors $\underline{\epsilon} \in \mathscr{D}_\epsilon$ and $\underline{\gamma} \in \mathscr{D}_\gamma$, respectively. The bounded and closed domains $\mathscr{D}_\epsilon, \mathscr{D}_\gamma \subset \mathbb{R}^p$ contain admissible parameter vectors ensuring the strict positivity of the resulting coefficients.

3 Inversion of Diffusion Coefficient

This section focuses on inferring the diffusion coefficient γ from boundary measurements $\Lambda_{\gamma^*}(g)$ for suitable boundary conditions $g \in C^\infty(\partial Q)$. Note that according to Theorem 1, our original problem requires the spatial boundary conditions to be non-negative. The Calderón problem is usually formulated for all boundary conditions $g \in C^\infty(\partial Q)$. However, due to the invariance to constant shifts in the boundary data, the statements employed in the following still hold when only considering non-negative boundary conditions.

3.1 Data without Measurement Noise

In this subsection, we consider the data space $\mathscr{V}_y := \mathscr{L}(H^{\frac{1}{2}}(\partial Q), H^{-\frac{1}{2}}(\partial Q))$ and the data $y := \Lambda_{\gamma^*}$. We seek to reconstruct the diffusion coefficient causing the data y based on the relation

$$y = \mathscr{F}_c(\underline{\gamma}^*), \tag{6}$$

with forward response $\mathscr{F}_c : \mathscr{D}_\gamma \to \mathscr{V}_y, \underline{\gamma} \mapsto \Lambda_\gamma$. Hence, the solution of the classical inverse problem is defined as

$$\underline{\gamma} = \arg\min_{\hat{\underline{\gamma}} \in \mathscr{D}_\gamma} \|\mathscr{F}_c(\hat{\underline{\gamma}}) - y\|, \tag{7}$$

where $\|\cdot\|$ denotes the operator norm. The injectivity of the Calderón DN map is essential for the well-posedness of the classical inverse problem in the following theorem.

Theorem 3. *Let $Q \subset \mathbb{R}^2$ be a bounded Lipschitz domain and let $\omega : [0, \delta] \to \mathbb{R}$ be a function with $\omega(a) \le |\log(a)|^{-\beta}$ for some $\beta > 0$ and $\delta > 0$ sufficiently small. Then the classical inverse problem for the diffusion coefficient is well-posed, that is the minimization problem (7) has a unique solution and if $\|\Lambda_\gamma - \Lambda_{\gamma^*}\|$ is sufficiently small, the following stability bound holds:*

$$\|\gamma - \gamma^*\|_{L^\infty(Q)} \le C\omega(\|\Lambda_\gamma - \Lambda_{\gamma^*}\|) \le C|\log(\|\Lambda_\gamma - \Lambda_{\gamma^*}\|)|^{-\beta}. \tag{8}$$

Proof. The existence and uniqueness of the solution follow from the injectivity of the DN map. For the proof of the stability bound, we refer to Barceló et al. [2] □

Similar non-logarithmic results for space dimensions $n \ge 3$ can be found in [13, Section 5.3].

Numerical framework. To formulate a computable version of the minimization problem (7), we consider a triangulation Q_h of Q with refinement parameter $\mathsf{h} > 0$ and $N \in \mathbb{N}$ vertices, of which $N_B < N$ lie on the boundary. In the following, we consider the problem only on Q_h and define the normal vectors in the boundary vertices to coincide with the normal vectors of Q in those points. We approximate the solution of the boundary value problem from Lemma 2 using a finite element (FE) method in the first order linear Lagrange space S_h which is well-established for elliptic problems, see for example [14, Chapter 3]. The discretized solution can be represented as

$$v_\mathsf{h} = \sum_{i=1}^{N} \underline{v}_i \varphi_i, \tag{9}$$

with the FE solution vector $\underline{v} := (\underline{v}_i)_{i=1}^N \in \mathbb{R}^N$ and $\{\varphi_i\}_{i=1}^N$ being a basis of hat-functions of S_h. Then we define the discretized DN map as

$$\Lambda_{\gamma,\mathsf{h}}(g) := \gamma \partial_\nu v_\mathsf{h}|_{\partial Q_\mathsf{h}}. \tag{10}$$

Note that this map is also linear and continuous with respect to g as both of these properties transfer to the

subspace $S_\mathsf{h}(Q_\mathsf{h}) \subset H^1(Q_\mathsf{h})$. Assuming the data are also discretized as $y_\mathsf{h} := \Lambda_{\gamma^*,\mathsf{h}}$, we obtain the relation

$$y_\mathsf{h} = \mathscr{F}_\mathsf{h}(\underline{\gamma}^*), \tag{11}$$

where the discretized forward response $\mathscr{F}_\mathsf{h}$ employs the discretized DN map $\Lambda_{\gamma,\mathsf{h}}$ instead of Λ_γ. Thus, the minimization problem (7) can be discretized as

$$\underline{\gamma} \in \arg\min_{\underline{\hat{\gamma}} \in \mathscr{D}_\gamma} \|\mathscr{F}_\mathsf{h}(\underline{\hat{\gamma}}) - y_\mathsf{h}\|. \tag{12}$$

The stability bound from Theorem 3 becomes

$$\begin{aligned}\|\gamma - \gamma^*\|_{L^\infty(Q_\mathsf{h})} \leq C|\log\big(&\|\Lambda_\gamma - \Lambda_{\gamma,\mathsf{h}}\| + \|\Lambda_{\gamma,\mathsf{h}} - \Lambda_{\gamma^*,\mathsf{h}}\| \\ &+ \|\Lambda_{\gamma^*} - \Lambda_{\gamma^*,\mathsf{h}}\|\big)|^{-\beta},\end{aligned} \tag{13}$$

provided that the argument of the logarithm is sufficiently small. The approximation errors $\|\Lambda_\gamma - \Lambda_{\gamma,\mathsf{h}}\|$ and $\|\Lambda_{\gamma^*} - \Lambda_{\gamma^*,\mathsf{h}}\|$ tend to zero as $h \to 0$ when considering a family of quasi uniform triangulations as the FE solution v_h converges towards the weak solution v, see [3, Chapter 2.7]. Our numerical approach to solve the inverse problem aims at minimizing the term $\|\Lambda_{\gamma,\mathsf{h}} - \Lambda_{\gamma^*,\mathsf{h}}\|$. As the operator norm is not numerically accessible, we derive an upper bound in the following which we minimize instead. For this, we approximate the boundary data

$$g \approx g_\mathsf{h} := \sum_{j=1}^{N_B} \underline{g}_j \hat{\varphi}_j, \tag{14}$$

with the coefficient vector $\underline{g} := (\underline{g}_j)_{j=1}^{N_B} \in \mathbb{R}^{N_B}$ for the representation with respect to the basis $\{\hat{\varphi}_j\}_{j=1}^{N_B}$ of hat-functions restricted to the boundary ∂Q_h. As the discretized DN map is linear and continuous with respect to g, the following estimate holds:

$$\|\Lambda_{\gamma,\mathsf{h}}(g) - \Lambda_{\gamma,\mathsf{h}}(g_\mathsf{h})\|_{L^2(Q_\mathsf{h})} \leq \|\Lambda_{\gamma,\mathsf{h}}\| \|g - g_\mathsf{h}\|_{L^2(Q_\mathsf{h})}. \tag{15}$$

The first factor is finite for every $h > 0$ and cannot grow arbitrarily large since $\|\Lambda_{\gamma,\mathsf{h}}\| - \|\Lambda_\gamma\| \leq \|\Lambda_{\gamma,\mathsf{h}} - \Lambda_\gamma\| \to 0$ as $h \to 0$. The second factor represents the approximation error between the boundary data and its interpolation in the corresponding FE space. We consider the discretized operator norm

$$\|\Lambda_{\gamma,\mathsf{h}} - \Lambda_{\gamma^*,\mathsf{h}}\|_\mathsf{h} := \sup_{\|g_\mathsf{h}\|_{L^2(\partial Q_\mathsf{h})}=1} \|(\Lambda_{\gamma_\mathsf{h},h} - \Lambda_{\gamma^*,\mathsf{h}})(g_\mathsf{h})\|_{L^2(\partial Q_\mathsf{h})}, \tag{16}$$

which we can bound from above according to the following lemma.

Lemma 4. *Let $\{\hat{\varphi}_j\}_{j=1}^{N_B}$ be the nodal FE basis at the boundary. Let $\lambda_{min}^\mathsf{h} > 0$ be the smallest eigenvalue of the mass matrix $M := (\langle\hat{\varphi}_i, \hat{\varphi}_j\rangle)_{i,j=1}^{N_B}$. Then we obtain*

$$\|\Lambda_{\gamma,\mathsf{h}} - \Lambda_{\gamma^*,\mathsf{h}}\|_\mathsf{h} \leq \frac{1}{\sqrt{\lambda_{min}^\mathsf{h}}} \sum_{j=1}^{N_B} \|(\Lambda_{\gamma,\mathsf{h}} - \Lambda_{\gamma^*,\mathsf{h}})(\hat{\varphi}_j)\|_{L^2(\partial Q_\mathsf{h})}. \tag{17}$$

The proof is provided in the supplementary material. Note that λ_{min}^h might decrease when refining the grid but is independent of the choice of the diffusion coefficient. Thus we may omit this positive scaling constant during the minimization.

Definition 5. Let us denote $\mathscr{F}_\mathsf{h}^j(\underline{\gamma}) := \mathscr{F}_\mathsf{h}(\gamma)(\hat{\varphi}_j)$ and $y_\mathsf{h}^j := y_\mathsf{h}(\hat{\varphi}_j)$ for $j = 1, \ldots, N_B$. We consider the target function $\hat{\mathsf{f}}_\mathsf{h} : \mathscr{D}_\gamma \to \mathbb{R}_0^+$ which is defined as

$$\hat{\mathsf{f}}_\mathsf{h}(\underline{\gamma}) := \sum_{j=1}^{N_B} \|\mathscr{F}_\mathsf{h}^j(\underline{\gamma}) - y_\mathsf{h}^j\|_{L^2(\partial Q_\mathsf{h})}. \tag{18}$$

Then $\underline{\hat{\gamma}} \in \mathscr{D}_\gamma$ is a solution to the discretized inverse problem for the diffusion coefficient if it satisfies

$$\hat{\mathsf{f}}_\mathsf{h}(\underline{\hat{\gamma}}) = \min_{\underline{\gamma} \in \mathscr{D}_\gamma} \hat{\mathsf{f}}_\mathsf{h}(\underline{\gamma}). \tag{19}$$

If the domain $\mathscr{D}_\gamma$ is compact, then there exists a solution of the minimization problem (19), however we cannot guarantee uniqueness and stability anymore in the discretized setting.

Implementation. The two main tasks are computing evaluations of the target function $\hat{\mathsf{f}}_\mathsf{h}$ and solving the corresponding minimization problem. Our implementation uses the open-source finite element library FEniCS Project [1]. We construct the triangulation Q_h by defining a triangular mesh with resolution $r_c > 0$ [2] on the polygonal approximation of $Q \subset \mathbb{R}^2$ with N_c boundary segments. This mesh can be generated using the CGAL [3] algorithm. We define a linear Lagrange FE space on this mesh. For evaluating the target function, the evaluations of the forward response $\mathscr{F}_\mathsf{h}^j$, $j = 1, \ldots, N_B$ need to be computed. To render these evaluations more efficient, we employ an offline-online decomposition. The offline phase is executed once prior to the actual inversion process and precomputes all reusable, parameter-independent components. During the online phase, the remaining parameter-dependent quantities are computed for a given parameter vector. The key advantage of this approach emerges when the target function needs to be evaluated multiple times for varying

[1] FEniCS Project: `https://fenicsproject.org`
[2] Notation from FEniCS `mshr`, larger values yield finer meshes.
[3] The CGAL Project: `https://doc.cgal.org`.

parameter vectors since it reuses precomputable components. Assuming the parametric diffusion coefficient can be represented by the set of functions $\{\tilde{\varphi}_k\}_{k=1}^p$, that is $\gamma = \sum_{k=1}^p \underline{\gamma}_k \tilde{\varphi}_k$, we obtain for $\underline{\gamma} \in \mathscr{D}_\gamma$:

$$\mathscr{F}_\mathsf{h}^j(\underline{\gamma}) = \Big(\sum_{k=1}^p \underline{\gamma}_k \; \tilde{\varphi}_k\Big)|_{\partial Q_\mathsf{h}} \Big(\sum_{i=1}^N \underline{v}_i^j \; \nabla\varphi_i|_{\partial Q_\mathsf{h}} \cdot \mathbf{n}\Big). \quad (20)$$

We mark the quantities which can be precomputed during the offline phase in darker gray while the lighter gray boxes mark the parameter-dependent quantities. The outwards pointing normal vector $\mathbf{n}$ on the boundary ∂Q_h is piecewise constant and we obtain the gradient of the hat functions via automatic differentiation provided by FEniCS. Note that the inner product with the normal vector $\mathbf{n}$ automatically performs the restriction to the boundary ∂Q_h. Furthermore, the restriction of the diffusion coefficient to the boundary is incorporated automatically during the construction of the target function when computing the $L^2(\partial Q_\mathsf{h})$-norm using FEniCS's built-in numerical integration. The FE solution vector $\underline{v}^j \in \mathbb{R}^N$ can be determined by solving the linear system $A_\gamma \underline{v}^j = \underline{b}^j$ where the matrix A_γ is given by

$$(A_\gamma)_{l,i} := \begin{cases} \delta_{l,i} & \text{if } l \text{ on boundary} \\ \int_{Q_\mathsf{h}} \gamma \nabla\varphi_i \cdot \nabla\varphi_l \, dx & \text{otherwise} \end{cases} \quad (21)$$

for $l,i = 1,...,N$ and $\underline{b}^j$ is the j-th unit vector due to $\{\hat{\varphi}_j\}_{j=1}^{N_B}$ being nodal. As the boundary value problem is elliptic, there exists a unique solution $\underline{v}^j$. Furthermore, we also consider an offline-online decomposition for assembling the system matrix. For this, we precompute the parameter-independent matrices

$$A_k := \Big(\int_{Q_\mathsf{h}} \tilde{\varphi}_k \nabla\varphi_i \cdot \nabla\varphi_l\Big)_{l,i=1}^N, \quad (22)$$

for $k = 1,...,p$ using standard DOLFIN [4] functions. During the online phase, a preliminary representation $\tilde{A}_\gamma$ of the system matrix A_γ before enforcing the boundary conditions can be computed as

$$\tilde{A}_\gamma = \sum_{k=1}^p \underline{\gamma}_k \; A_k. \quad (23)$$

Based on this, the true system matrix A_γ can be obtained using built-in functions provided by DOLFIN. Since the hat-functions are a nodal basis, we expect the resulting system matrix A_γ to be sparse. For numerical efficiency, we thus convert this matrix into SciPy's [5] compressed sparse column (CSC) format. To solve the linear system efficiently, we employ the LU-decomposition of the sparse system matrix and then solve the system using the supernodal sparse LU algorithm provided by SciPy. We precompute the data $y_\mathsf{h}^j = \mathscr{F}_\mathsf{h}^j(\gamma^*)$ for $j = 1,...,N_B$ during the offline phase. Algorithm 6 summarizes our approach for evaluating the target function at a given parameter vector $\underline{\gamma} \in \mathscr{D}_\gamma$. The offline and online phases are highlighted again in dark and light gray, respectively. During the inversion process, we minimize the target function which leads to a constrained p-dimensional minimization problem. We expect the computational cost to increase drastically with increasing parameter space dimension p. For solving the minimization problem, we consider SciPy's l-BFGS-B method which is a gradient-based Quasi-Newton method. Since we do not provide an analytical gradient of the target function, SciPy approximates this gradient numerically employing a two-point finite difference scheme. Furthermore, box constraints can be imposed, ensuring that we restrict our search to the domain of admissible parameters if $\mathscr{D}_\gamma$ is a p-dimensional box.

Algorithm 6 (**Target function evaluation**).

initialize mesh, FE space S_h, functions $\tilde{\varphi}_1,...,\tilde{\varphi}_p$
determine and store $\mathbf{n}$ for all facets
assemble $\underline{b}^j$ and $\underline{A}_k$ for $j = 1,...,N_B, k = 1,...,p$

For given parameter vector $\underline{\gamma}$ do:

set $\gamma := \sum_{k=1}^p \underline{\gamma}_k \tilde{\varphi}_k$ and $\hat{\mathfrak{f}}_\mathsf{h} := 0$
assemble A_γ and compute LU-decomposition
for $j = 1,...,N_B$ **do**
    solve $A_\gamma \underline{v}^j = \underline{b}^j$
    compute $\mathscr{F}_\mathsf{h}^j(\underline{\gamma})$ based on $\underline{\gamma}$ and $\underline{v}^j$
    compute $\mathfrak{f}^j := \|\mathscr{F}_\mathsf{h}^j(\underline{\gamma}) - y_\mathsf{h}^j\|_{L^2(\partial Q_\mathsf{h})}$
    update $\hat{\mathfrak{f}}_\mathsf{h} += \mathfrak{f}^j$
end for

Numerical results. All numerical experiments are conducted on an AMD Ryzen™ 5 5625U processor with 16.00 GB installed RAM and twelve logical processors. When parallelization is possible, we conduct experiments on six of the processors. We consider $Q \subset \mathbb{R}^2$ to be the unit disc and define two meshes covering this domain. Mesh A has $N_c = 30$ boundary segments and the resolution $r_c = 6.50$, leading to $N = 100$ vertices of which $N_B = 30$ are on the boundary. The specifications for mesh B are $N_c = 35$, $r_c = 15.33$, $N = 500$ and $N_B = 70$. In the following, we consider the diffusion coefficient

$$\gamma(x) := \underline{\gamma}_1 + \underline{\gamma}_2 x_1^2, \quad (24)$$

[4] DOLFIN: Part of the FEniCS Project[1].
[5] SciPy: `https://scipy.org`

for $x = (x_1, x_2)^\top \in \mathbb{R}^2$ with the parameter vector $\underline{\gamma} := (\underline{\gamma}_1, \underline{\gamma}_2)^\top \in \mathbb{R}^2$. Furthermore, we set $\mathscr{D}_\gamma := [0.1, 10.0]^2$ and $\underline{\gamma}^* := (1.0, 2.0)^\top$. Throughout this section, we generate the measurement data for the Calderón problem separately from the measurements regarding the PME. Figure 2 illustrates the unknown diffusion coefficient γ^*. The initial guess for the l-BFGS-B method is generated randomly from the uniform distribution on $\mathscr{D}_\gamma$ and we use an error tolerance of 1×10^{-6}. For better comparison, we use the same initial guess for the experiments on both meshes. Table 1 contains the corresponding numerical results rounded to four decimal points and the computation time. We observe that our scheme is able to reconstruct the parameter vector accurately up to the considered precision.

Table 1 – Classical inversion of diffusion coefficient.

Experiment	Mesh A	Mesh B
reconstructed $\underline{\gamma}$	$\begin{pmatrix}1.0000\\2.0000\end{pmatrix}$	$\begin{pmatrix}1.0000\\2.0000\end{pmatrix}$
time [s]	7.74	20.23

Overall, we have seen that the infinite-dimensional inverse problem from Equation (7) is well-posed. However, well-posedness cannot be guaranteed for the discretized version. In the following, we aim to introduce some measurement noise to our data, introducing further uncertainties in our model. Thus, we turn to Bayesian inversion to obtain a well-posed discretized inverse problem even with noisy data.

3.2 Data with Measurement Noise

When working with noisy data, the injectivity of the Calderón DN map does not necessarily guarantee the well-posedness of the classical inverse problem anymore, even before discretization. Therefore, we consider a Bayesian inversion approach in this section which addresses the uncertainty introduced by the measurement noise by treating all variables as random variables on a complete probability space $(\Omega, A, \mathbb{P})$. Their distributions reflect the uncertainty in both the data and the model. In contrast to the classical inversion, the solution of the inverse problem is no single estimate of the unknown variable but a probability distribution capturing the full range of possible values and their likelihoods. Let $\underline{\Gamma} : \Omega \to \mathbb{R}^p$ denote the random variable modelling the parameter vector of the diffusion coefficient and let $Y : \Omega \to \mathbb{R}^M$ be the random variable modelling the measurement data such that

$$Y = \mathscr{F}_b(\underline{\Gamma}) + \Xi. \tag{25}$$

The random variable $\Xi : \Omega \to \mathbb{R}^M$ represents the independent measurement noise with distribution $\mathbb{P}_\xi$. We consider the discrete data space $\mathcal{V}_y := \mathbb{R}^M$ with $M := N_B(N_B - 1)$ and the forward response $\mathscr{F}_b : \mathbb{R}^p \to \mathbb{R}^M$ with

$$\mathscr{F}_b(\underline{\gamma}) := \begin{bmatrix} \left(\Lambda_{\gamma,\mathrm{h}}(\hat{\varphi}_1)(x_\mathrm{m})\right)_{\mathrm{m}=1}^{N_B-1} \\ \vdots \\ \left(\Lambda_{\gamma,\mathrm{h}}(\hat{\varphi}_{N_B})(x_\mathrm{m})\right)_{\mathrm{m}=1}^{N_B-1} \end{bmatrix}, \tag{26}$$

where $\{x_\mathrm{m}\}_{\mathrm{m}=1}^{N_B-1}$ are the midpoints of the boundary facets of Q_h. We emphasize that this forward map is already discretized. In contrast to section 3.1, the subscript b does not represent a refinement parameter but merely indicates that the quantity is used in Bayesian inversion. Note that we only lose information through the point evaluations of the diffusion coefficient as the remaining terms of the discretized DN map are constant within each boundary facet. The Bayesian inversion idea illustrated in Figure 3 can be summarized as follows: We start with an initial belief about $\underline{\Gamma}$ which is encoded in the prior distribution $\mathbb{P}_0$. This belief is updated by additional information obtained via the observation $Y = y$ of the measurement data and encoded in the posterior distribution $\mathbb{P}_y$. The posterior distribution represents the solution of the Bayesian inverse problem and can be characterized using Bayes' theorem. In the following,

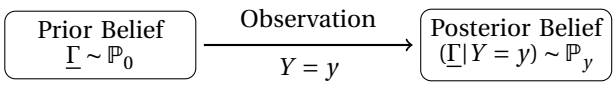

Figure 3 – Bayesian inversion idea.

we assume $\underline{\Gamma}$ and Ξ to be absolutely continuous with respect to the Lebesgue measure. The Radon-Nikodym theorem yields the existence of probability density functions ρ_ξ and ρ_0, respectively.

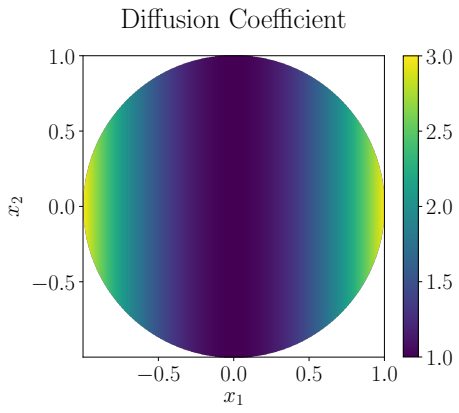

Figure 2 – Quadratic diffusion coefficient.

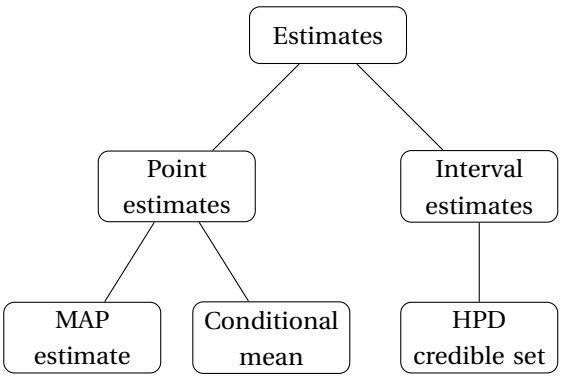

Figure 4 – Overview of considered estimates.

Definition 7. Let $\mathscr{D}_\gamma \subset \mathbb{R}^p$ be a compact domain of admissible parameter vectors, $|\mathscr{D}_\gamma| > 0$ and let the observation $Y = y$ be given. We consider a uniform prior on $\mathscr{D}_\gamma$ and Gaussian noise with covariance $\sigma^2 \mathrm{I}, \sigma^2 > 0$. Then the solution to the Bayesian inverse problem is the posterior distribution with density

$$\rho_y(\underline{\gamma}) = \frac{1}{\Theta_y} \exp(-\frac{1}{2\sigma^2} \|y - \mathscr{F}_b(\underline{\gamma})\|_2^2) \rho_0(\underline{\gamma}), \tag{27}$$

for almost all $\underline{\gamma} \in \mathbb{R}^p$ and with a suitable normalizing constant $\Theta_y > 0$.

This inverse problem is already discretized and thus computable in practice. The problem's well-posedness remains to be examined.

Theorem 8. *The inverse problem from Definition 7 is weak, Hellinger and total-variation well-posed. For any* $1 \leq \mathscr{P} < \infty$, *it is also Wasserstein($\mathscr{P}$) well-posed.*

Proof. As the forward response $\mathscr{F}_b$ is continuous with respect to $\underline{\gamma}$, it is also measurable. For the proof of the continuity, we refer to the supplementary material. Furthermore, the uniform density on the compact domain $\mathscr{D}$ has a finite $\mathscr{P}$-th moment for any $1 \leq \mathscr{P} < \infty$. Latz [15] yields the asserted well-posedness statements. □

Estimates. In contrast to the classical inversion, we are able to obtain two fundamentally different types of estimates: point estimates and interval estimates. While point estimates yield a single vector containing a reasonable reconstruction of the unknown parameter vector $\underline{\gamma}^*$, interval estimates provide regions which contain the unknown parameter vector with a certain probability according to our stochastic model. Figure 4 contains the estimates which we consider in the following. For the point estimates, we consider the maximum a posteriori (MAP) estimate which is defined as

$$\underline{\gamma}_{MAP} \in \arg\max_{\underline{\gamma} \in \mathbb{R}^p} \rho_y(\underline{\gamma}) \tag{28}$$

and the conditional mean (CM) which is given by

$$\underline{\gamma}_{CM} := \mathbb{E}[\underline{\Gamma} | Y = y] = \int_{\mathbb{R}^p} \underline{\gamma} \rho_y(\underline{\gamma}) \, d\underline{\gamma}. \tag{29}$$

In our case regarding the Bayesian inversion of the diffusion coefficient, both a CM and MAP estimate exist due to the continuity of the posterior density within the compact support and the fact that the prior has a finite first moment. To avoid the potentially high-dimensional integration for the CM, we consider the Monte Carlo estimator

$$\underline{\Gamma}_{MC}(N_s) := \frac{1}{N_s} \sum_{\mathfrak{n}=0}^{N_s-1} \underline{\Gamma}_{\mathfrak{n}} \tag{30}$$

to approximate $\underline{\gamma}_{CM}$ where $(\underline{\Gamma}_{\mathfrak{n}})_{\mathfrak{n}=0}^{N_s-1}$ is a sequence of $N_s \in \mathbb{N}$ independent copies of the random vector $\underline{\Gamma} | Y = y$. The Monte Carlo estimator converges $\mathbb{P}_y$-almost surely to the CM for $N_s \to \infty$. This follows from the strong law of large numbers. As the posterior has a finite second moment, the convergence rate is $N_s^{-\frac{1}{2}}$. We can obtain sample based realizations of the Monte Carlo estimator by drawing N_s samples $\{\underline{\gamma}_{\mathfrak{n}}\}_{\mathfrak{n}=1}^{N_s-1} \subset \mathbb{R}^p$ from the posterior and computing the sample mean. This can be done using Markov chain Monte Carlo methods such as the Metropolis-Hastings algorithm which allows sampling from the posterior without explicit knowledge of the normalizing constant Θ_y. For the interval estimates, we consider the highest posterior density (HPD) credible set which is defined for the credibility $1-\alpha$, $\alpha \in (0,1)$ as

$$E_{cr} := \{\underline{\gamma} \in \mathbb{R}^p : \rho_y(\underline{\gamma}) \geq \kappa(\alpha)\}, \tag{31}$$

with $\kappa(\alpha) > 0$ being the largest constant such that the set E_{cr} satisfies the following condition:

$$\mathbb{P}_y(E_{cr}) \geq 1 - \alpha. \tag{32}$$

It provides the smallest region which contains the unknown parameter vector $\underline{\gamma}^*$ with a certain credibility. This means that according to our stochastic model, the posterior distribution assigns this region the probability $1-\alpha$. If the posterior density is free of constant plateaus, then the HPD credible set is unique. Figure 5 shows the 95% credible set for an exemplary real-valued random variable with a bimodal probability density. For approximately Gaussian posteriors, we propose a sample-based approximation of the HPD credible set as

$$\hat{E}_{cr} = \left\{\underline{\gamma} \in \mathbb{R}^p : (\hat{\underline{\gamma}} - \underline{\gamma})^\top \hat{\Sigma}^{-1} (\hat{\underline{\gamma}} - \underline{\gamma}) \leq \Phi^{\leftarrow}_{\chi^2_p}(1-\alpha)\right\}, \tag{33}$$

where $\hat{\underline{\gamma}}$ and $\hat{\Sigma}$ are the sample mean and covariance, respectively, and $\Phi^{\leftarrow}_{\chi^2_p}$ denotes the generalized inverse of the χ^2 distribution with p degrees of freedom. To

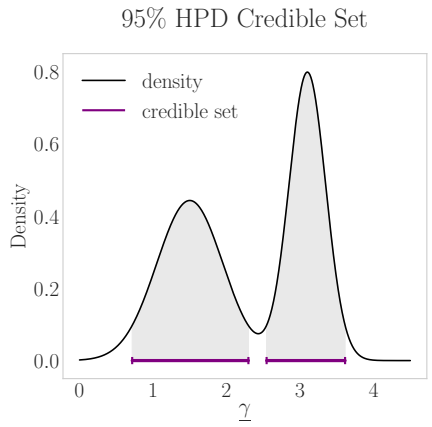

Figure 5 – Exemplary 95% HPD credible set for bimodal probability density.

improve the readability, we omit the dependence on the number N_s of samples in our notation. If the posterior is exactly Gaussian, then the credible ellipsoid fulfills

$$\mathbb{P}_y(\underline{\gamma} \in \hat{E}_{cr}) \to 1-\alpha \quad \text{for} \quad N_s \to \infty. \tag{34}$$

The proof mainly relies on the fact that the squared Mahalanobis distance asymptotically follows the χ^2_p-distribution and that the empirical distribution converges to the posterior provided it is indeed Gaussian.

Implementation. In the following, we focus on the implementation of evaluating the forward map $\mathcal{F}_b$ and computing the point and interval estimates. We do not discuss the implementation of the sampling method in detail as there already exists an abundance of comprehensive literature, see for example [18]. When evaluating the forward map, we exclusively work with point evaluations instead of functions, enabling the vectorization of our computations and enhancing the parameter separability. Using the same notation as in the previous section, our goal now is to compute the evaluations

$$\begin{aligned}\mathcal{F}_b(\underline{\gamma})_{j;m} &:= \Lambda_{\gamma,\mathrm{h}}(\hat{\varphi}_j)(x_\mathfrak{m}) \\ &= \Big(\sum_{k=1}^{p} \underline{\gamma}_k \; \tilde{\varphi}_k(x_\mathfrak{m})\Big)\Big(\sum_{i=1}^{N} \underline{v}_i^j \; \nabla\varphi_i(x_\mathfrak{m})\cdot\mathbf{n}_\mathfrak{m}\Big),\end{aligned} \tag{35}$$

for $j = 1,\dots,N_B$ and $\mathfrak{m} = 1,\dots,N_B-1$. Again, the quantities precomputable during the offline phase are highlighted in dark gray and the parameter-dependent quantities which need to be computed during the online phase are marked by the light gray boxes. The midpoints $x_\mathfrak{m}, \mathfrak{m} = 1,\dots,N_B-1$ and the normal vectors $\mathbf{n}_\mathfrak{m} := \mathbf{n}(x_\mathfrak{m})$ can be determined via built-in FEniCS operations. For enhancing the readability of the subsequent steps, we define the following parameter-independent matrices and vectors

$$\begin{aligned}\Phi_\mathfrak{m} &:= (\tilde{\varphi}_k(x_\mathfrak{m}))_{k=1}^{p} && \in \mathbb{R}^{p} \\ \Phi_{evals} &:= (\Phi_1,\dots,\Phi_{N_B-1}) && \in \mathbb{R}^{p\times(N_B-1)} \\ \Psi_\mathfrak{m} &:= (\nabla\varphi_i(x_\mathfrak{m})\cdot\mathbf{n}(x_\mathfrak{m}))_{i=1}^{N} && \in \mathbb{R}^{N} \\ \Psi_{evals} &:= (\Psi_1,\dots,\Psi_{N_B-1}) && \in \mathbb{R}^{N\times N_B-1}.\end{aligned} \tag{36}$$

To compute Ψ_{evals}, we first generate the FE basis functions $\varphi_i, i = 1,\dots,N$ explicitly by defining functions in the FE space whose coefficient vectors correspond to the unit vectors $e_i, i = 1,\dots,N$. FEniCS provides access to the gradients of the basis functions via automatic differentiation but does not allow point evaluations of those gradients because of the discontinuities at the element facets. As a remedy, we project each component of the gradient onto a discontinuous Galerkin space of order zero in which we are able to perform the desired evaluations in the midpoints of the boundary facets. Since the components of the gradient are locally constant, this does not change the values of the desired evaluations. Furthermore, we consider the row-vectors $\Lambda_{evals,j} := (\mathcal{F}_b(\underline{\gamma})_{j;1},\dots,\mathcal{F}_b(\underline{\gamma})_{j;N_B-1}) \in \mathbb{R}^{1\times(N_B-1)}$ forming the forward map $\mathcal{F}_b(\underline{\gamma}) := ((\Lambda_{evals,j})^\top)_{j=1}^{N_B} \in \mathbb{R}^{N_B(N_B-1)}$. Thus we obtain

$$\mathcal{F}_b(\underline{\gamma})_{j;m} = \underline{\gamma}^\top \; \Phi_\mathfrak{m} \; (\underline{v}^j)^\top \; \Psi_\mathfrak{m}. \tag{37}$$

If we let the operator $\odot$ denote the element-wise multiplication of two matrices of the same dimension, then we get the vectorized formulation

$$\Lambda_{evals,j} = \underline{\gamma}^\top \; \Phi_{evals} \odot (\underline{v}^j)^\top \; \Psi_{evals}. \tag{38}$$

Compared to the classical inversion approach, the current evaluation-based scheme and the resulting parameter separability allow us to shift a major portion of the required computations to the offline phase. During the online phase, we only have to determine the FE solution vector $\underline{v}^j$ for given parameter vector $\underline{\gamma}$ and boundary condition $\hat{\varphi}_j$. The evaluations of the forward map can then be obtained by matrix-vector operations. Our approach is summarized in Algorithm 9.

Lastly, we discuss the computation of the point and interval estimates. Regarding the point estimates, we are interested in the CM and MAP estimate. For obtaining the MAP estimate, we maximize the log-posterior $\ell_y = \log(\rho_y)$ for simplicity, neglecting additive constants. As before, we employ the l-BFGS-B method for the numerical optimization and set the box constraints to $\mathcal{D}_\gamma$ assuming it is a p-dimensional box. For the CM, we draw samples from the posterior distribution via the random-walk Metropolis-Hastings algorithm, testing

Algorithm 9 (**Forward map evaluation ($\mathscr{F}_b$)**).

initialize mesh, FE space S_h and DG space S_{DG}
initialize functions $\tilde{\varphi}_1, ..., \tilde{\varphi}_p$
determine $x_\mathfrak{m}$ and $\mathbf{n}_\mathfrak{m}$ for $\mathfrak{m} = 1, ..., N_B - 1$
compute Ψ_{evals} and Φ_{evals}
assemble $\underline{b}^j$ and $\underline{A}_k$ for $j = 1, ..., N_B, k = 1, ..., p$

For given parameter vector $\underline{\gamma}$ do:

compute $\underline{\gamma}_{evals} = \underline{\gamma}^\top \Phi_{evals}$
assemble A_γ and compute LU-decomposition
for $j = 1, ..., N_B$ **do**
    solve $A_\gamma \underline{v}^j = \underline{b}^j$
    compute $\Lambda_{evals,j} = \underline{\gamma}_{evals} \odot (\underline{v}^j)^\top \Psi_{evals}$
    store corresponding elements in $\mathscr{F}_b(\underline{\gamma})$
end for

different proposal covariances and selecting a suitable burn-in phase. These samples can then be employed to obtain a realization of the Monte Carlo estimator which approximates the CM. Python's multiprocessing[6] module allows us to generate multiple realizations of the Monte Carlo estimator in parallel. The generated samples can also be used to obtain approximations of the HPD credible sets. In the following, we restrict our considerations to the case $p = 2$ for simplicity but higher dimensions of the parameter space are also possible. For deriving a more convenient representation of $\hat{E}_{cr}$ from equation (33) in practice, we consider the eigendecomposition $\hat{\Sigma}^{-1} = Q\Delta_s Q^\top$ of the inverse sample covariance matrix where $\Delta_s = \mathrm{diag}(\lambda_1^{-1}, \lambda_2^{-1})$ and Q contains the eigenvectors of the sample covariance matrix. Here, $\lambda_1, \lambda_2 > 0$ represent the eigenvalues of the matrix $\hat{\Sigma}$. Through this eigendecomposition and a coordinate transform to a system with origin at the sample mean $\hat{\underline{\gamma}}$ and coordinate axes corresponding to the eigenvectors contained in Q, we can conclude: The approximate HPD credible set is an ellipse with main axes corresponding to the eigenvectors of the sample covariance matrix and center $\hat{\underline{\gamma}}$. Its main axes have the length $(\lambda_i \Phi^{\leftarrow}_{\chi^2_2}(1-\alpha))^{\frac{1}{2}}$ for $i = 1, 2$. Both the eigenvalues and the eigenvectors of the sample covariance matrix can be calculated using standard NumPy linear algebra functions. We use SciPy's inverse cumulative distribution function to determine the value $\Phi^{\leftarrow}_{\chi^2_p}(1-\alpha)$.

Numerical results. We repeat our previous numerical experiments in the Bayesian inversion setting. Thus we consider the same diffusion coefficient and the same domain $\mathscr{D}_\gamma$ as before but we generate noisy data with a variance of $\sigma^2 = 0.1$. Our goal in the following is to compute the sample based approximations of the CM estimate and the HPD credible set. For enhancing the numerical stability, we consider the log-posterior for the random-walk Metropolis-Hastings algorithm and we generate the initial state randomly from the uniform distribution on $\mathscr{D}_\gamma$. We employ the same initial state for the experiments on both meshes. The proposal covariance $\sigma^2_{\mathrm{prop}}\mathrm{I}$ for the random walk, the length of the burn-in phase and the number of generated samples for the experiments on both meshes can be found in Table 2. It also contains the approximation of the CM which is a less accurate but still reasonable reconstruction of $\underline{\gamma}^*$ than in the previous experiments. This is to be expected due to the introduced measurement noise. Figure 6 shows the approximate 95% HPD credible sets for the experiments on both meshes. Increasing the mesh refinement seems to decrease the set's size significantly, indicating a lower uncertainty in our second estimate.

In conclusion, we have formulated a discretized inverse problem which incorporates both measurement noise and prior information and is well-posed with respect to certain metrics. Thus we can reconstruct the diffusion coefficient once we have obtained the required boundary data according to Lemma 2. Having obtained estimates of the diffusion coefficient, we move on to the inversion of the porosity coefficient in the following section where we may treat the diffusion coefficient as a known quantity. Thus, we only have to solve the original IBVP based on the PME for the porosity coefficient and not for both coefficients simultaneously.

4 Inversion of Porosity Coefficient

Having examined different approaches for the inversion of the diffusion coefficient in the previous section, this section focuses on the inversion of the porosity coefficient. A particular advantage of our overall strategy is the decoupling of the inversion of the coefficients γ and ϵ. Therefore, we may assume in this section that the

Table 2 – Bayesian inversion of diffusion coefficient.

Experiment	Mesh A	Mesh B
σ^2_{prop}	1×10^{-3}	1×10^{-3}
length of burn-in	1000	1000
number of samples	10000	10000
acceptance rate	0.58	0.16
reconstructed $\underline{\gamma}$	$\begin{pmatrix}1.0423\\1.9896\end{pmatrix}$	$\begin{pmatrix}0.9929\\2.0010\end{pmatrix}$
time [s]	19.37	105.07

[6] https://docs.python.org/3/library/multiprocessing.html

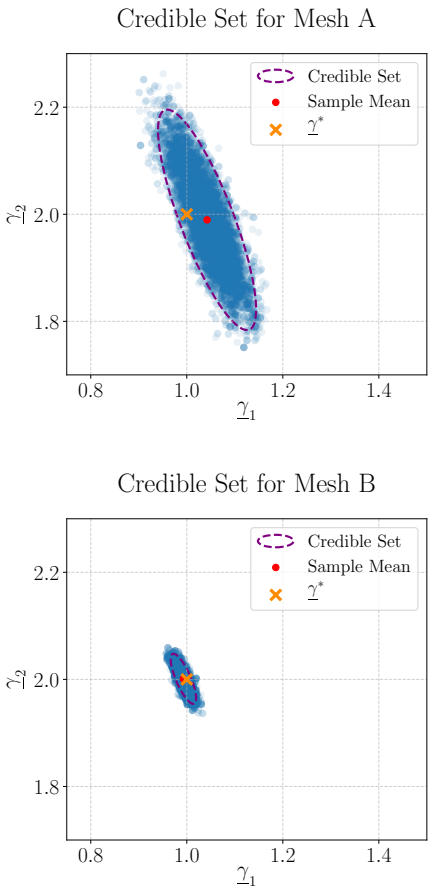

Figure 6 – 95% credible sets for the diffusion coefficient.

diffusion coefficient is already known. While we are able to work with the Calderón DN map Λ_γ for the diffusion coefficient, we must now consider the DN map $\Lambda^{PME}_{\epsilon,\gamma}$ based on the PME which is a time-dependent degenerate parabolic problem instead of an elliptic one. Unfortunately, this prohibits the use of the well-posedness results from section 3. In the following, we provide a method based on the previous Bayesian inversion framework, highlighting its practical implementation and computational strategies. We leave the matter of obtaining theoretical results open for future research.

Numerical framework. We consider the same triangulation Q_h of the spatial domain and the equidistant, discrete time-steps $0 = t_0 \leq t_1 \leq \ldots \leq t_{N_T} = T, N_T \in \mathbb{N}$, with step size Δt. Since the DN map is numerically not accessible, we work with the discretized PME DN map

$$\Lambda^{PME}_{\epsilon,\gamma,\mathrm{h}}(\phi) := \gamma \partial_\nu u^m_\mathrm{h}|_{[0,T)\times\partial Q_\mathrm{h}}, \tag{39}$$

where the function u_h represents a discretized solution of the PME. To solve the PME numerically, we employ a finite difference scheme in time and a FE scheme in space which is based on the weak formulation

$$\int_{Q_\mathrm{h}} \epsilon \frac{u^\mathfrak{n}_\mathrm{h}(x) - u^{\mathfrak{n}-1}_\mathrm{h}(x)}{\Delta t}\varphi_0 + \gamma \nabla (u^\mathfrak{n}_\mathrm{h}(x))^m \cdot \nabla \varphi_0 \, dx = 0 \tag{40}$$

in each time-step $t_\mathfrak{n}, \mathfrak{n} = 1, \ldots, N_T$ with test functions $\varphi_0 \in C^\infty_0(Q_\mathrm{h})$ and separately enforced boundary conditions. For better readability, we omit the space-dependence of ϵ, γ and φ_0 in our notation but highlight the fact that the functions $u^\mathfrak{n}_\mathrm{h} := u_\mathrm{h}(t_\mathfrak{n}, \cdot)$ for $\mathfrak{n} = 1, \ldots, N_T$ are discretized in time. As a preparation, we also define the discretized boundary conditions

$$\phi_j := \chi \hat{\varphi}_j^{\frac{1}{m}} \tag{41}$$

for $j = 1, \ldots, N_B$ where $\{\hat{\varphi}_j\}_{j=1}^{N_B}$ again denotes the basis of hat functions on ∂Q_h. In the following, we consider a fixed function χ satisfying the assumptions of Theorem 1. In contrast to the Calderón DN map, the DN map of the PME is not linear with respect to the boundary data. Thus, our ansatz does not guarantee a provably accurate approximation of $\Lambda^{PME}_{\epsilon,\gamma,\mathrm{h}}(\phi)$ solely by the span of $\{\Lambda^{PME}_{\epsilon,\gamma,\mathrm{h}}(\phi_j)\}_{j=1}^{N_B}$. Nevertheless, we choose this strategy as a practical compromise in view of the computational complexity of the problem at hand. To obtain a fully discrete data space, we consider point evaluations on the shell of the space time cylinder. For the Bayesian inversion, we model the parameter vector of the porosity coefficient as a random variable $\underline{\mathscr{E}}: \Omega \to \mathbb{R}^p$. The relation between $\underline{\mathscr{E}}$ and the random variable $Y : \Omega \to \mathbb{R}^{\bar{M}}$ describing the data is given by

$$Y = \mathscr{F}_e(\underline{\mathscr{E}}) + \Xi, \tag{42}$$

where the random variable $\Xi : \Omega \to \mathbb{R}^{\bar{M}}$ again represents the measurement noise. We consider the discrete data space $V_y := \mathbb{R}^{\bar{M}}$ with $\bar{M} := N_B N_T (N_B - 1)$ and the forward response $\mathscr{F}_e : \mathbb{R}^p \to \mathbb{R}^{\bar{M}}$ with

$$\mathscr{F}_e(\underline{e}) := \begin{bmatrix} \left(\Lambda^{PME}_{\epsilon,\gamma,\mathrm{h}}(\phi_1)(t_1, x_\mathfrak{m})\right)_{\mathfrak{m}=1}^{N_B-1} \\ \vdots \\ \left(\Lambda^{PME}_{\epsilon,\gamma,\mathrm{h}}(\phi_1)(t_{N_T}, x_\mathfrak{m})\right)_{\mathfrak{m}=1}^{N_B-1} \\ \vdots \\ \left(\Lambda^{PME}_{\epsilon,\gamma,\mathrm{h}}(\phi_{N_B})(t_{N_T}, x_\mathfrak{m})\right)_{\mathfrak{m}=1}^{N_B-1} \end{bmatrix} \tag{43}$$

with $x_\mathfrak{m}, \mathfrak{m} = 1, \ldots, N_B - 1$ denoting the midpoints of the boundary facets of Q_h and $t_\mathfrak{n}, \mathfrak{n} = 1, \ldots, N_T$ being the discrete time steps.

Definition 10. Let $\mathscr{D}_\epsilon \subset \mathbb{R}^p$ be a compact domain of admissible parameter vectors, $|\mathscr{D}_\epsilon| > 0$ and let the observation $Y = y$ be given. We consider a uniform prior

on $\mathscr{D}_\epsilon$ and Gaussian noise with covariance $\sigma^2\mathrm{I}, \sigma^2 > 0$. Then the solution to the Bayesian inverse problem for the porosity coefficient is the posterior distribution with density

$$\rho_y(\underline{\epsilon}) = \frac{1}{\Theta_y}\exp(-\frac{1}{2\sigma^2}\|y - \mathscr{F}_e(\underline{\epsilon})\|_2^2)\rho_0(\underline{\epsilon}), \tag{44}$$

for almost all $\underline{\epsilon} \in \mathbb{R}^p$ and with a suitable normalizing constant $\Theta_y > 0$.

Theorem 11. *Let $m \in \mathbb{N}$ be an odd number, let the numerical solution of the PME in each time step be obtained using the Newton method and let the initial guess be chosen such that the Newton method converges. If the time step size Δt is sufficiently small, then the numerical scheme is well-defined and the inverse problem from Definition 10 is weak, Hellinger and total-variation well-posed. For any $1 \le \mathscr{P} < \infty$, it is also Wasserstein($\mathscr{P}$) well-posed.*

Proof. In the supplementary material, we prove that the numerical scheme is well-defined and that the forward response $\mathscr{F}_e$ is continuous with respect to $\underline{\epsilon}$. The remaining proof is analogous to the proof of Theorem 8. □

To obtain point and interval estimates regarding the unknown parameter vector $\underline{\epsilon}$, we proceed analogously to section 3.2 but consider the new forward response $\mathscr{F}_e$. For the sample-based approximations of the CM and HPD credible set, we again draw samples from the posterior using the random walk Metropolis-Hastings algorithm with proposal covariance $\sigma^2_{\text{prop}}\mathrm{I}, \sigma^2_{\text{prop}} > 0$.

Implementation. For simplicity, we restrict our considerations to the exponent $m = 3$ in the following implementation. Other exponents are also possible and would require an element-wise exponentiation with $m-1$ instead of the element-wise squaring used in the subsequent derivations. Similar to before, we assume the porosity coefficient to be of the form $\epsilon = \sum_{k=1}^p \underline{\epsilon}_k \tilde{\varphi}_k$ with a suitable set of smooth functions $\{\tilde{\varphi}_k\}_{k=1}^p$. For evaluating the forward map $\mathscr{F}_e$ in some $\underline{\epsilon} \in \mathscr{D}_\epsilon$, we need to compute the evaluations

$$\begin{aligned}\mathscr{F}_e(\underline{\epsilon})_{j;\mathfrak{n};\mathfrak{m}} &:= \Lambda^{PME}_{\epsilon,\gamma,\mathfrak{h}}(\phi_j)(t_\mathfrak{n}, x_\mathfrak{m}) \\ &= 3\gamma(x_\mathfrak{m})u_\mathfrak{h}(t_\mathfrak{n}, x_\mathfrak{m})^2\nabla u_\mathfrak{h}(t_\mathfrak{n}, x_\mathfrak{m})\cdot\mathbf{n}_\mathfrak{m}.\end{aligned} \tag{45}$$

for $j = 1,...,N_B, \mathfrak{n} = 1,...,N_T$ and $\mathfrak{m} = 1,...,N_B - 1$. As before, our goal is to formulate an approach based on an offline-online decomposition. Reducing the computational effort of the online phase is particularly important as we need to solve N_T nonlinear systems of equations for each evaluation of the forward map which is expected to increase the complexity significantly. For better readability of the following steps, we introduce some notations. The discretized solution $u_\mathfrak{h}$ of the PME with boundary condition ϕ_j is of the form

$$u_\mathfrak{h}(t_\mathfrak{n}, \cdot) = \sum_{i=1}^N \underline{u}_i^{j,\mathfrak{n}}\varphi_i(\cdot), \tag{46}$$

where the coefficient vector $\underline{u}^{j,\mathfrak{n}} = (\underline{u}_i^{j,\mathfrak{n}})_{i=1}^N \in \mathbb{R}^N$ corresponds to the FE solution vector in the $\mathfrak{n}$-th time step with boundary condition $\phi_j(t_\mathfrak{n}, \cdot)$. We collect evaluations of reusable components in the vectors and matrices

$$\begin{aligned}\Phi_\mathfrak{m} &:= (\bar{\varphi}_k(x_\mathfrak{m}))_{k=1}^p &&\in \mathbb{R}^p, \\ \Phi_{evals} &:= (\Phi_1, ..., \Phi_{N_B-1}) &&\in \mathbb{R}^{p\times N_B-1}, \\ \Psi_\mathfrak{m} &:= (\gamma(x_\mathfrak{m})\nabla\varphi_i(x_\mathfrak{m})\cdot\mathbf{n}_\mathfrak{m})_{i=1}^N &&\in \mathbb{R}^N, \\ \Psi_{evals} &:= (\Psi_1, ..., \Psi_{N_B-1}) &&\in \mathbb{R}^{N\times N_B-1}.\end{aligned} \tag{47}$$

Since we assume that the diffusion coefficient γ is already known from previous experiments, we incorporate its evaluations in the vector $\Psi_\mathfrak{m}$ and we denote $\gamma_\mathfrak{m} := \gamma(x_\mathfrak{m})$. In addition, we also define the matrix $\underline{U}^j := (\underline{u}^{j,1}, ..., \underline{u}^{j,N_T}) \in \mathbb{R}^{N\times N_T}$ consisting of the FE solution vectors of all time steps. Finally, we denote by $\odot$ the element-wise multiplication and by $(\cdot)^{\circ 2}$ the element-wise squaring of two matrices or vectors. Hence we obtain

$$\begin{aligned}\mathscr{F}_e(\underline{\epsilon})_{j;\mathfrak{n};\mathfrak{m}} &= 3\Big(\sum_{i=1}^N \underline{u}_i^{j,\mathfrak{n}}\varphi_i(x_\mathfrak{m})\Big)^2\Big(\gamma_\mathfrak{m}\sum_{i=1}^N \underline{u}_i^{j,\mathfrak{n}}\nabla\varphi_i(x_\mathfrak{m})\cdot\mathbf{n}_\mathfrak{m}\Big) \\ &= 3\big(\Phi_\mathfrak{m}^\top\underline{u}^{j,\mathfrak{n}}\big)^2\Psi_\mathfrak{m}^\top\underline{u}^{j,\mathfrak{n}}.\end{aligned} \tag{48}$$

Considering multiple boundary facet midpoints at once, we define $\Lambda^\mathfrak{n}_{\epsilon,\gamma,\mathfrak{h}}(\phi_j) := \Big(\big(\mathscr{F}_e(\underline{\epsilon})_{j;\mathfrak{n};\mathfrak{m}}\big)_{\mathfrak{m}=1}^{N_B-1}\Big)^\top \in \mathbb{R}^{1\times N_B-1}$ which is given by

$$\Lambda^\mathfrak{n}_{\epsilon,\gamma,\mathfrak{h}}(\phi_j) = 3\Big(\big(\underline{u}^{j,\mathfrak{n}}\big)^\top\Phi_{evals}\Big)^{\circ 2}\odot\Big(\big(\underline{u}^{j,\mathfrak{n}}\big)^\top\Psi_{evals}\Big). \tag{49}$$

We identify $\Lambda^{PME}_{evals,j} := \Big(\Lambda^\mathfrak{n}_{\epsilon,\gamma,\mathfrak{h}}(\phi_j)\Big)_{\mathfrak{n}=1}^{N_T} \in \mathbb{R}^{N_T\times N_B-1}$ with

$$\Lambda^{PME}_{evals,j} = 3\Big(\big(\underline{U}^j\big)^\top\ \Phi_{evals}\Big)^{\circ 2}\odot\Big(\big(\underline{U}^j\big)^\top\ \Psi_{evals}\Big) \tag{50}$$

as the vectorized components of the forward map. The quantities marked by the dark gray boxes can be precomputed during the offline phase. Only the FE solution vectors forming the matrix $\underline{U}^j$ depend on the values of $\underline{\epsilon}$ and need to be computed during the online phase. For generating the functions $\hat{\varphi}_j, j = 1,...,N_B$ explicitly, we extract the indices of the vertices on the boundary and generate functions from the FE space $S_\mathfrak{h}(Q_\mathfrak{h})$ whose coefficient vectors are the unit vectors corresponding to

these indices. The restriction to the boundary is performed automatically in FEniCS when enforcing the boundary conditions. The main task of the online phase for evaluating the forward response $\mathcal{F}_e$ is to determine the FE solution vector for each boundary condition and each time step. In contrast to the Calderón PDE, the PME is a nonlinear equation. Thus, in each time-step a nonlinear system of equations needs to be solved which is computationally more expensive than solving a linear system. To do so, we employ the built-in Newton solver provided by FEniCS. Note that for computing the

Algorithm 12 (**Forward map evaluation** ($\mathcal{F}_e$))**.**

initialize mesh, FE space S_h and DG space S_{DG}
assemble functions $\hat{\varphi}_1, ..., \hat{\varphi}_{N_B}$
compute evaluations $\chi(t_1), ..., \chi(t_{N_T})$
determine $x_\mathfrak{m}$ and $\mathbf{n}_\mathfrak{m}$ for $\mathfrak{m} = 1, ..., N_B - 1$
compute Ψ_{evals} and Φ_{evals}

For given parameter vector $\underline{\epsilon}$ do:
assemble $\epsilon = \sum_{k=1}^{p} \underline{\epsilon}_k \tilde{\varphi}_k$
for $j = 1, ..., N_B$ **do**
  for $\mathfrak{n} = 1, ..., N_T$ **do**
    determine $\underline{u}^{j,\mathfrak{n}}$
    store corresponding elements in $\underline{U}^j$
  end for
  set $\Lambda^{PME}_{evals,j} = 3\left(\left(\underline{U}^j\right)^\top \Phi_{evals}\right)^{\circ 2} \odot \left(\left(\underline{U}^j\right)^\top \Psi_{evals}\right)$
  store corresponding elements in $\mathcal{F}_e(\underline{\epsilon})$
end for

forward response $\mathcal{F}_e(\underline{\epsilon})$ for given parameter vector $\underline{\epsilon}$, we do not only have to iterate over all boundary conditions ϕ_j, $j = 1, ..., N_B$ but also over all time steps which leads to a nested loop. This further contributes to the increase of computational effort when evaluating the forward response $\mathcal{F}_e$. For obtaining point and interval estimates, we proceed analogously to the previous section using the forward response $\mathcal{F}_e$ instead of $\mathcal{F}_b$. One major difference is that for the numerical approximation of the MAP estimate, we employ SciPy's gradient-free Powell minimization method instead of the l-BFGS-B method to enhance the numerical feasibility. Apart from this, we may reuse the implementation regarding the sample generation and approximation of the CM and HPD credible ellipse.

Numerical results. For our experiments regarding the porosity coefficient, we set $T = 1.5$ and consider a coarser mesh $\hat{A}$ and a finer mesh $\hat{B}$ using the spatial meshes A and B, as well as $N_T = 20$ and $N_T = 30$ time-steps, respectively. In the following, we choose the time-dependent part of the boundary conditions as

Table 3 – Bayesian inversion of porosity coefficient.

Experiment	Mesh $\hat{A}$	Mesh $\hat{B}$
proposal covariance	1×10^{-3}	1×10^{-3}
burn-in	1000	1000
number of samples	10000	10000
acceptance rate	0.93	0.89
reconstructed $\underline{\epsilon}$	$\begin{pmatrix}1.7284\\5.5010\end{pmatrix}$	$\begin{pmatrix}2.2149\\4.9451\end{pmatrix}$
time [s]	54475.97	358168.65

$$\chi(t) = \begin{cases} 0 & t \le 0.5, \\ 0.5\sin\big(2\pi(t-0.75)\big) + 0.5 & t \in (0.5, 1), \\ 1 & t \ge 1. \end{cases} \tag{51}$$

Although this function is not an element of $C^\infty([0,\infty))$, which is theoretically required for the injectivity of the DN map in Theorem 1, this does not affect our approach since χ only enters through evaluations in the discrete time steps $t_1, ..., t_{N_T}$. We consider the porosity coefficient

$$\epsilon(x) = \underline{\epsilon}_1 + \underline{\epsilon}_2 x_1^2 \tag{52}$$

for $x = (x_1, x_2)^\top \in \mathbb{R}^2$ with true parameter vector $\underline{\epsilon}^* = (2.0, 5.0)^\top$. The resulting porosity coefficient ϵ^* is depicted in Figure 7. Furthermore, we set $\mathcal{D}_\epsilon := [1.0, 4.0] \times [3.5, 6.5]$ and we assume the diffusion coefficient to be known from our previous experiments. Similar to before, we consider the noise variance to be $\sigma^2 = 0.1$ and employ the random walk Metropolis-Hastings method for the sample generation. The remaining specifications of the experiments are given in Table 3 which also contains the resulting approximated CM estimate. Compared to the previous experiments, we observe a decreased

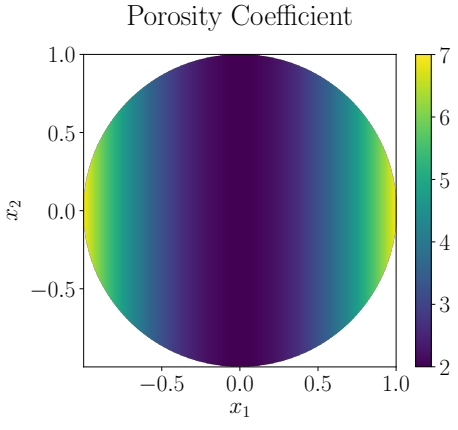

Figure 7 – Quadratic porosity coefficient

accuracy of our reconstructions of $\underline{\epsilon}^*$. This may be attributed to the problem being more challenging or to a slower convergence of the Markov chain. Furthermore, the computation time is also significantly higher which is to be expected as the forward map is more expensive to evaluate, see Algorithm 12. Figure 8 shows the approximated 95% HPD credible sets for the experiments on both meshes. The set's size decreases when refining

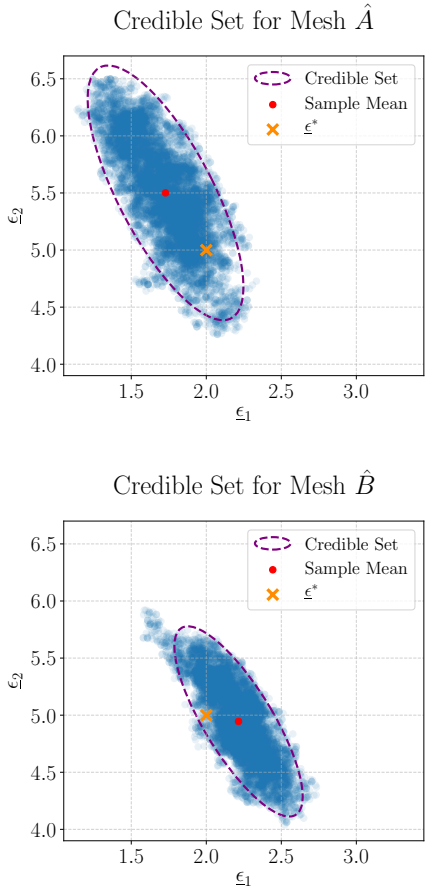

Figure 8 – 95% credible sets for the porosity coefficient.

the mesh, indicating lower uncertainty in this estimate, and the reconstruction of $\underline{\epsilon}^*$ becomes more accurate which is consistent with expected convergence trends. Overall, we observe a substantially longer computation time which emphasizes the practical benefits of our decoupled inversion strategy, avoiding the simultaneous sampling of both the porosity and diffusion coefficient.

5 Summary

We have formulated a novel inversion strategy which decouples the inversion of the diffusion and porosity coefficient and relates the inversion of the former to the Calderón problem. Exploiting the properties of the Calderón problem, we have derived a classical inverse problem for noise-free data which is well-posed prior to discretization. To incorporate measurement noise, we have considered a Bayesian inversion approach. The resulting discretized inverse problem is well-posed with respect to certain metrics and allows for uncertainty quantification. A practical advantage is the possibility to vectorize the problem and to apply an offline-online decomposition. We also have transferred the Bayesian inversion setting to solve the original IBVP for the porosity coefficient, although the well-posedness of this scheme is yet to be fully explored. While our approach lays the foundation for solving the IBVP for the PME numerically, it serves as an initial framework which can be refined and extended in several areas to improve its reliability. This includes examining the Calderón data generation from lemma 2 for finite times $T < \infty$, examining triangulations of the space domain Q better capturing the smooth boundary and exploring alternative, established solvers for the PME. Furthermore, we could drop the assumption that ϵ and γ are parametric and instead approximate them in a suitable finite-dimensional space, introducing an additional approximation error.

Code Availability: Both, the LaTeX source code as well as the python-script for the simulation, are available as supplementary material and can be obtained under the DOI: 10.5281/zenodo.17140634

Supplemental Material: This manuscript contains a Supplemental Material appendix.

CRediT authorship contribution statement: *Lea Blessing*: Conceptualization, Methodology, Formal analysis, Investigation, Software, Visualization, Writing – original draft. *Andrea Barth*: Conceptualization, Methodology, Supervision, Writing – review and editing.

References

[1] Kari Astala and Lassi Päivärinta. A boundary integral equation for Calderón's inverse conductivity problem. *Collectanea Mathematica*, 57:127–139, 2006.

[2] Juan A. Barceló, Tomeu Barceló, and Alberto Ruiz. Stability of the inverse conductivity problem in the plane for less regular conductivities. *Journal of Differential Equations*, 173(2):231–270, 2001.

[3] Dietrich Braess. *Finite Elemente: Theorie, schnelle Löser und Anwendungen in der Elastizitätstheorie*. Masterclass. Springer Berlin Heidelberg, 5 edition, 2013.

[4] Tommi Brander. Calderón problem for the p- Laplacian: First order derivative of conductivity on the boundary. *Proceedings of the American Mathematical Society*, 144(1):177–189, 2016.

[5] Martin Brühl and Martin Hanke. Numerical implementation of two noniterative methods for locating inclusions by impedance tomography. *Inverse Problems*, 16(4):1029–1042, 2000.

[6] Alberto Calderón. On an inverse boundary value problem. *Computational & Applied Mathematics*, 25:133–138, 2006.

[7] Cătălin I. Cârstea, Tuhin Ghosh, and Gen Nakamura. An inverse boundary value problem for the inhomogeneous porous medium equation. *SIAM Journal on Applied Mathematics*, 85 (1):278–293, 2025.

[8] Yuki Daido, Hyeonbae Kang, and Gen Nakamura. A probe method for the inverse boundary value problem of non-stationary heat equations. *Inverse Problems*, 23(5):1787, 2007.

[9] Fabrice Delbary, Per Christian Hansen, and Kim Knudsen. Electrical impedance tomography: 3d reconstructions using scattering transforms. *Applicable Analysis*, 91(4):737–755, 2012.

[10] Ali Feizmohammadi and Lauri Oksanen. An inverse problem for a semi-linear elliptic equation in Riemannian geometries. *Journal of Differential Equations*, 269(6):4683–4719, 2020.

[11] Avner Friedman. *Partial differential equations of parabolic type*. Prentice-Hall Series in Modern Analysis. Courier Dover Publications, 2008.

[12] Victor Isakov. Uniqueness of recovery of some quasilinear partial differential equations. *Communications in Partial Differential Equations*, 26(11-12):1947–1973, 2001.

[13] Victor Isakov. *Inverse Problems for Partial Differential Equations*, volume 127 of *Applied Mathematical Sciences*. Springer Cham, 2017.

[14] Peter Knabner and Lutz Angermann. *Numerical Methods for Elliptic and Parabolic Partial Differential Equations*, volume 44 of *Texts in Applied Mathematics*. Springer New York, 2003.

[15] Jonas Latz. On the well-posedness of Bayesian inverse problems. *SIAM/ASA Journal on Uncertainty Quantification*, 8: 451–482, 2020.

[16] Adrian I. Nachman. Global uniqueness for a two-dimensional inverse boundary value problem. *Annals of Mathematics*, 143: 71–96, 1996.

[17] Gen Nakamura and Haibing Wang. Linear sampling method for the heat equation with inclusions. *Inverse Problems*, 29: 104015, 2013.

[18] Christian P. Robert and George Casella. *Monte Carlo Statistical Methods*. Springer Texts in Statistics. Springer New York, 2004.

[19] Ben Schweizer. *Partielle Differentialgleichungen: Eine anwendungsorientierte Einführung*. Springer Berlin Heidelberg, Berlin, Heidelberg, 2023.

[20] John Sylvester and Gunther Uhlmann. A global uniqueness theorem for an inverse boundary value problem. *Annals of Mathematics*, 125(1):153–169, 1987.